Discrete time crystal made of topological edge magnons

Dhiman Bhowmick,[1] Hao Sun,[2] Bo Yang,[1] and Pinaki Sengupta[1]
[1]*School of Physical and Mathematical Sciences, Nanyang Technological University, Singapore 639798, Singapore*
[2]*The Institute for Functional Intelligent Materials (I-FIM), National University of Singapore, 4 Science Drive 2, Singapore 117544, Singapore*

(Received 7 September 2022; revised 8 July 2023; accepted 10 July 2023; published 31 July 2023)

We report the emergence of time-crystalline behavior in the π-Berry phase protected edge states of a Heisenberg ferromagnet in the presence of an external driving field. The magnon amplification due to the external field spontaneously breaks the discrete time-translational symmetry, resulting in a discrete time crystal with a period that is twice that of the applied electromagnetic field. We discuss the nature and symmetry protection of the time crystalline edge states and their stability against various perturbations that are expected in real quantum magnets. We propose an experimental signature to unambiguously detect the time crystalline behavior and identify two recently discovered quasi-two-dimensional magnets as potential hosts. We present a realization of time crystals at topological edge states, which can be generalized and extrapolated to other bosonic quasiparticle systems that exhibit parametric pumping and topological edge states.

DOI: 10.1103/PhysRevB.108.014434

I. INTRODUCTION

Symmetries and symmetry breaking underlie many interesting phases and phenomena in condensed matter physics. A crystal with a periodic array of atoms/molecules is a simple example where continuous symmetry in space is spontaneously broken. Based on Lorentz invariance that puts spatial and temporal coordinates on equal footing, Wilczek in 2012 proposed the idea of a time crystal [1], where time translation symmetry can also be spontaneously broken in the ground state of a quantum many body system—local observables oscillate in time with fixed periodicity, analogous to the spatial modulation in crystalline solids. However, despite Lorentz invariance, space and time are not completely interchangeable, as evidenced by their different signs in the metric tensor. Moreover, by its very own definition, the ground state or any equilibrium state of a closed quantum system does not vary with time and Wilczek's original idea was shown to be unfeasible [2–6]. Nevertheless the idea of time crystals as new phases of matter has generated much interest over the past decade. More recent studies have established that time crystals can emerge under proper conditions. It is now widely accepted that time crystals can be realized in out-of-equilibrium systems [5,7–11] and particularly in the presence of a periodic driving field.

Time crystals have been theoretically studied and experimentally reported in a range of systems, including magnons [12,13], ultracold atoms [14,15], superfluid quantum gas [15,16], and qubits [17–19]. Different time crystals can be broadly categorized in two categories: continuous time crystal [20–23] and discrete time crystal [24–26]. Discrete time crystalline behavior in a periodically driven system is characterized by the local properties that oscillate in time with a period which is a multiple of that of the driving field [12–16,24–45]. In many cases, the driving field injects energy into the system that eventually leads to thermalization. The periodic behaviors before thermalization are known as prethermal time crystals [27–31]. Conversely, if the driving frequency is much larger than the local energy scales or if heat generated during thermalization can be dissipated, a driven dissipative time crystal can form because thermalization takes a long time [40–44,46]. For Floquet many body localized (MBL) systems [24–26], where absence of coupling between different energy eigenstates prevent thermalization of the states, a more robust long-lived time crystal can be realized. However, MBL phase requires a strong disorder, which is practically not feasible to prepare experimentally. Thus a research effort is still ongoing to find new more efficient and effective ways for stabilizing the many body phase time crystal which is much more unstable than its counterpart space crystals.

In this work, we show that a discrete time crystal can emerge in the topological π-Berry phase protected magnon edge state of a quantum magnet driven by a periodic field in absence of any time reversal symmetry breaking interactions (see Fig. 1). The topological protection of the edge state strongly reduces the scattering of edge magnons. In contrast to Floquet MBL, our proposal avoids the need for strong disorder, which stands in the way of experimental realization in larger systems [11]. We work with a realistic microscopic Hamiltonian that captures the low-energy magnetic properties of the quasi-two-dimensional (2D) quantum magnets haydeeite and Cu(1,3-bdc). The topological time-crystal considered in this study should not be confused with the Floquet topological time crystal studied in Refs. [47,48], because the topology in the latter systems is out of equilibrium phenomena, whereas the topology in our system is intrinsic to the system which ensures the stability of time crystal. While we have demonstrated the emergence of time crystalline state in magnons on the kagome lattice, the results are applicable to other bosonic quasiparticles like phonons, plasmons, polaritons, etc., where parametric amplification has been demonstrated [49–59] and topological edge states are also present [60–74].

 ©2023 American Physical Society

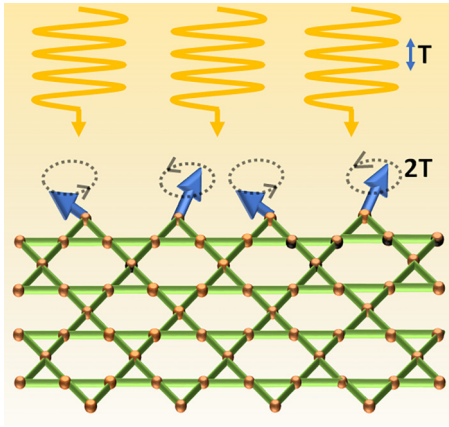

FIG. 1. Realization of a discrete time crystal made of topological edge magnons. At the edge spins oscillate with a period twice that of the external EM field, breaking discrete time translational symmetry. The phases of oscillation for neighboring sites are opposite as the magnons are amplified at the $k = \pi$ point

II. DISCRETE TIME CRYSTAL

We consider the ferromagnetic Heisenberg model on a kagome lattice,

$$\mathcal{H}_0 = -J \sum_{ij} \hat{S}_i \cdot \hat{S}_j. \tag{1}$$

The low energy magnon excitations above the ferromagnetic ground states are described by the linear spin-wave theory: $\hat{S}_i^+ = \sqrt{2S}\hat{a}_i$, $\hat{S}_i^- = \sqrt{2S}\hat{a}_i^\dagger$, and $\hat{S}_i^z = S - \hat{a}_i^\dagger \hat{a}_i$, where S denotes the magnitude of the spin and $\hat{a}_i^\dagger(\hat{a}_i)$ creates (annihilates) a magnon at site i. Application of the above transformation to $\mathcal{H}_0$ yields a tight binding magnon Hamiltonian where the interactions are neglected. The resulting band structure for a ribbon geometry [Fig. 2(a)] is shown in Fig. 2(b). The bulk bands carry a nontrivial quantized $\mathbb{Z}_2$ topological invariant (Zak phase or π-Berry phase) and contain nearly flat topological edge states between the projected Dirac points [75,76]. Any effective time reversal symmetry breaking terms in the Hamiltonian, such as the Dzyaloshinskii-Moriya interaction (DMI), would open up a gap in the magnon spectrum at the Dirac points [77] and imparts dispersion to the edge states at $k = \pi$, destroying discrete time crystalline behavior that is discussed later in Sec. III.

As bosons not subject to the Pauli exclusion principle, magnons normally populate the bottom of the band, far from the edge states. However, recent studies have shown that edge state magnons can be controllably amplified at arbitrary energies by tailored electromagnetic (EM) waves [78]. The EM field with amplitude $\boldsymbol{E}$ and frequency Ω couples to the magnetic insulators via polarization [79–81] as

$$H_c = \cos(\Omega t)\boldsymbol{E} \cdot \sum_{\langle i,j \rangle} \boldsymbol{P}_{ij}, \tag{2}$$

where $\boldsymbol{P}_{ij}$ is the polarization operator of the magnetic insulator. The relevant terms in $\boldsymbol{P}_{ij}$ that contribute to magnon amplification consist of bilinear spin operators on the nearest

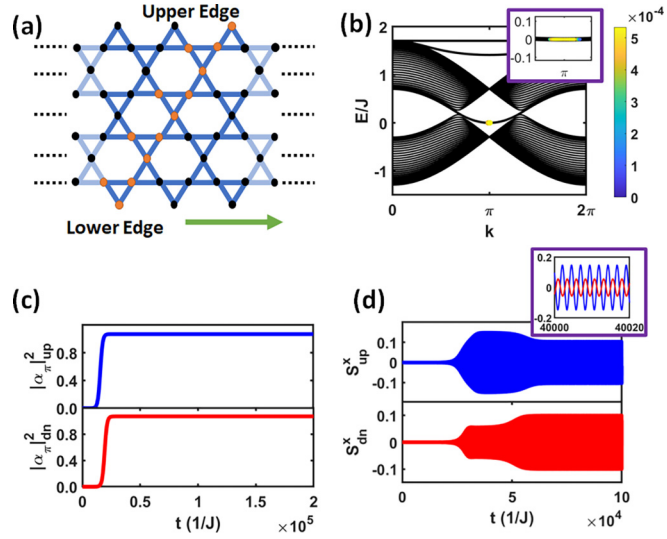

FIG. 2. (a) Schematic of a kagome ferromagnetic system with a finite number of sites along width (orange sites) and the system is periodic along the green arrow after a certain number of sites. (b) The magnon band structure is shown in black. The yellow dots denote the amplified topological edge magnonic states. Inset shows the magnified picture of the band near $k = \pi$ and the color code describes the value of the positive imaginary part of eigenvalues. (c) The number of magnons at $k = \pi$ as a function of time for upper (blue) and lower edge (red) states, indicating parametric amplification of edge magnons. (d) Time crystal made of topological edge magnons reflected in oscillation of in-plane spin component S^x at a site at upper (blue plot) and lower edges (red plot). Inset shows the magnified figure within a particular time limit. The period of oscillation is twice that of the external EM field. The parameters used for all the plots are $J = 1.0$, $\gamma = 5 \times 10^{-4}$, $\eta = 9 \times 10^{-4}$, $\Omega = 5.1716$, $p_0 = 1.0$, $E_0^x = 0.0$, and $E_0^y = 0.002$.

neighbor bonds (see Appendix A),

$$\mathbf{P}_{ij} \approx \boldsymbol{p}_{0,ij}(\mathbf{S}_i \cdot \mathbf{Q}_{ij})(\mathbf{S}_j \cdot \mathbf{Q}_{ij}). \tag{3}$$

Other polarization terms are not important for this study as they will be neglected in the rotating wave approximation [78]. Furthermore, we have neglected the effect of the magnetic field component of the electromagnetic wave for the following reasons. The magnetic field couples with the system in a form of Zeeman coupling which carries a term proportional to $\cos(\Omega t)$ and is only able to couple with the magnons of energy Ω. Thus the edge magnons remain unaffected which has a frequency of $\Omega/2$ (see later in this section). Bulk magnons are also less affected by magnetic field, as discussed in Appendix F.

The equation of motion for the magnon field $\tilde{\alpha}_k$ is given by (see Appendix B for more details)

$$\frac{d}{dt}\begin{pmatrix} \tilde{\alpha}_k^* \\ \tilde{\alpha}_{-k} \end{pmatrix} = \mathrm{i}\begin{pmatrix} \tilde{\epsilon}_k - \mathrm{i}\frac{\gamma\mathbb{I}+\eta|\alpha_k|^2}{2} & \frac{[\tilde{H}_c]_{12}}{2} \\ -\frac{[\tilde{H}_c]_{21}}{2} & -\tilde{\epsilon}_{-k} - \mathrm{i}\frac{\gamma\mathbb{I}+\eta|\alpha_k|^2}{2} \end{pmatrix}\begin{pmatrix} \tilde{\alpha}_k^* \\ \tilde{\alpha}_{-k} \end{pmatrix}, \tag{4}$$

where $(\tilde{\alpha}_k^* \ \tilde{\alpha}_{-k})$ represent the magnon fields $\langle \hat{\tilde{a}}_{n,k} \rangle$; $\tilde{\epsilon}_k$ is a diagonal matrix with elements $\epsilon_{n,k} - \frac{\Omega}{2}$, where $\epsilon_{n,k}$ is the energy eigenvalue; γ and η are phenomenological linear and

nonlinear damping constants; $\mathbb{I}$ is the identity matrix and $|\alpha_k|^2$ is the diagonal matrix with entries $|\langle\hat{\tilde{a}}_{n,k}\rangle|^2$. The subscripts n and k are band index and reciprocal space point, respectively. Moreover, $[\tilde{H}_c]_{12}$ is the off-diagonal elements of the coupling matrix in the eigenbasis (see Appendix B). The square matrix on the right hand side of Eq. (4) is the dynamical matrix with complex eigenvalues (for $\eta = 0$). The real and imaginary parts of the eigenvalues represent the energy and lifetime of the magnon, respectively. In the absence of EM coupling ($[\tilde{H}_c]_{12} \approx O_{N\times N}$), the imaginary part of the eigenvalues is negative indicating magnon decay. However, as the amplitude of the EM field increases the imaginary part of some of the eigenvalues satisfying $\epsilon_{n,k} + \epsilon_{n,-k} \approx \Omega$ becomes positive. This indicates the onset of spontaneous amplification of magnons. The yellow dots in the band structure [Fig. 2(b)] are the eigenvalues with positive imaginary part.

The solution of Eq. (4) describes amplified coherent magnons above a cutoff amplitude of the EM field [15,16,82,83]. Figure 2(c) shows the amplified coherent magnons population for the edge states of upper and lower edges at $k = \pi$ as a function of time. The presence of the nonlinear damping suppresses the exponential increase of the magnon number and the system reaches a steady state.

While the number of magnons ($|\langle\hat{\tilde{a}}_{n,k}\rangle|^2$) are identical in the rotating and the laboratory frames in the steady state (see Fig. 2), the field $\langle\hat{\tilde{a}}_{n,k}\rangle$ oscillates in time. Specifically when the pair of amplified magnons satisfy $\epsilon_{n,k} = \epsilon_{n,-k} = \Omega/2$, the steady state expectation values for the field in the rotating frame are independent of time, i.e., $\langle\hat{\tilde{a}}_{n,k}(t)\rangle^s_{\rm rot} = \langle\hat{\tilde{a}}_{n,k}\rangle^s_{\rm rot}$ (see Appendix D). Thus the fields in the two frames are related as

$$\langle\hat{\tilde{a}}_{n,k}(t)\rangle^{\rm s}_{\rm lab} \approx \langle\hat{\tilde{a}}_{n,k}\rangle^{\rm s}_{\rm rot} \exp\left(\mathrm{i}\frac{\Omega}{2}t\right), \tag{5}$$

where the superscript "s" denotes steady state expectation value.

The equation of motion (4) has a $\mathbb{Z}_2$ symmetry $\hat{\tilde{a}}_{n,k} \to -\hat{\tilde{a}}_{n,k}$. Above a critical amplitude of the EM field, the amplified magnon field at the edges of the system spontaneously breaks the $\mathbb{Z}_2$ symmetry by acquiring a finite, nonzero $\langle\hat{\tilde{a}}_{n,k}\rangle^{\rm s}_{\rm lab}$ that oscillates in time with a period which is twice that of the driving EM field. Thus a discrete time crystal of edge state magnons is formed via amplification [15,16] that breaks the discrete time translational symmetry spontaneously.

This time crystalline behavior can be experimentally observed by measuring the transverse magnetization at the edges, i.e., the spin components $\hat{S}^x_i$ and $\hat{S}^y_i$—the spin component $\hat{S}^z_i$ is constant, because it is related to the number of magnons $|\langle\hat{\tilde{a}}_{i,k}\rangle|^2$, which is invariant in time in the steady state. The x component of the spin, $\langle\hat{S}^x_i\rangle$, is given in terms of the fields $\langle\hat{\tilde{a}}_{n,k}\rangle^{\rm s}_{\rm rot}$ as

$$\begin{aligned}\langle\hat{S}^x_i\rangle = \sqrt{\frac{S}{2N_x}}\Bigg[&\sum_{k>0,n}[U_1^\dagger]_{in}\langle\hat{\tilde{a}}_{n,k}\rangle^{\rm s}_{\rm rot}e^{\frac{i\Omega t}{2}}e^{-ikx_i}\\ &+\sum_{k>0,n}[U_2^\dagger]_{in}\langle\hat{\tilde{a}}_{n,-k}\rangle^{\rm s}_{\rm rot}e^{\frac{i\Omega t}{2}}e^{ikx_i}\\ &+[U_1^\dagger]_{in}\langle\hat{\tilde{a}}_{n,0}\rangle^{\rm s}_{\rm rot}e^{\frac{i\Omega t}{2}}+\text{H.c.}\Bigg].\end{aligned} \tag{6}$$

Figure 2(d) demonstrates the oscillation of S^x_i at a site at the upper edge (blue) and the lower edge (red). The different k points arrive at a steady state at a different time (see Appendix C) and so S^x_i in Fig. 2(d) modulates transiently and reaches a steady state when all the amplified k points do. The oscillation amplitudes of $\langle\hat{S}^x_i\rangle$ at both edges are nearly identical, but they are not exactly equal, since it is a superposition of several fields $\langle\hat{\tilde{a}}_{n,k}\rangle^{\rm s}_{\rm rot}$ [see Eq. (6)]; while the magnitude of the fields $\langle\hat{\tilde{a}}_{n,k}\rangle^{\rm s}_{\rm rot}$ at two edges are the same, the phases are not. Moreover, the amplitude of oscillation varies with different simulations due to the random starting conditions representing the vacuum fluctuations [82,83]. Finally, time crystalline behavior also holds for the long-range order in spatial directions due to the coherence of the pumped magnon at $k = \pi$. Since the amplification of magnons extends over a finite momentum range around $k = \pi$, a spatial modulation in the amplitude of oscillation is expected.

III. SYMMETRY PROTECTION

Although a Heisenberg ferromagnet breaks time-reversal symmetry τ, the system still preserves effective time reversal symmetry $\tau_{\rm eff} = \mathcal{R}_\pi(\boldsymbol{n})\tau$, where $\mathcal{R}_\pi(\boldsymbol{n})$ is π rotation of spins around an $\boldsymbol{n}$ axis. This effective symmetry is useful to describe the system in the language of magnons [77]. The breaking of effective time reversal symmetry, which depends on both the direction of DMI and spin moments of a ferromagnetic ground state, is ubiquitous in many real quantum magnets, resulting in dispersive edge states. As a result, the condition, $\epsilon_{n,k} = \epsilon_{n,-k}$ for a pair of amplified magnons, as assumed above, is broken. Then, $\langle\hat{\tilde{a}}_{n,k}\rangle^s_{\rm rot}$ becomes time dependent and, according to Eq. (5), the period of oscillation of the fields at a particular k point will no longer be exactly twice the period of the external EM field. For a finite system, there will be a finite number of amplified points around $k = \pi$; adding over the fields at a few amplified points according to Eq. (6) would result in an oscillation of S^x that is incommensurate with the external field, resulting in a quasitime crystal [34]. In the thermodynamic limit, when the number of k points in the vicinity of $k = \pi$ diverges, the oscillation would become chaotic in nature, destroying the time-crystal-like behavior.

Here we demonstrate the absence of the time crystal, in the presence of time-reversal symmetry breaking DMI. We would like to emphasize that not all DMI breaks time-reversal symmetry. Breaking of time-reversal symmetry depends both on the direction of DMI and the direction of spin moments of a ferromagnetic ground state [77]. The model Hamiltonian in the absence of time-reversal symmetry becomes

$$\mathcal{H}_D = -J\sum_{ij}\hat{S}_i\cdot\hat{S}_j + D\sum_{ij}\hat{z}\cdot(\hat{S}_i\times\hat{S}_j) - B_z\sum_i\hat{S}^z_i, \tag{7}$$

where D and B_z are DMI and magnetic field perpendicular to the 2D-lattice plane. The breaking of the time-reversal symmetry opens up a gap in the bulk-magnon band and we get a dispersive edge magnon state. Thus the amplification is not only limited to the $k = \pi$ but other momentum points such that the relationship $\omega_k + \omega_{-k} = \Omega$ is satisfied, which is shown in Fig. 3(a). Moreover, the spin oscillation at the edges becomes chaotic in nature, as shown in Fig. 3(b). The reason behind this chaotic oscillation can be understood from

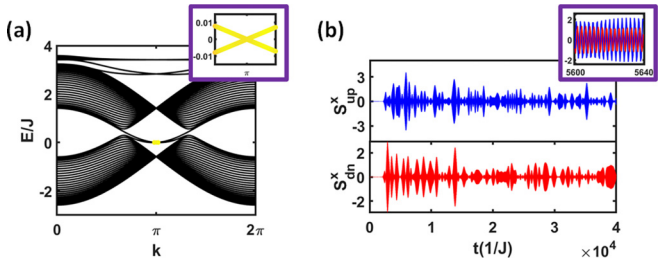

FIG. 3. (a) Magnon band structure in the presence of effective time reversal symmetry breaking DMI. The yellow dots denote amplified magnon eigenstates. Inset shows the magnified band near $k = \pi$. (b) A chaotic oscillation of spin component S^x at a site at the upper (blue plot) and lower (red plot) edges are shown, indicating the destruction of the time crystal. Insets show the magnified figures of the corresponding figures within a particular time limit. The parameters used for all the plots are $J = 1.0$, $D = 0.05$, $B_z \to 0^+$, $\gamma = 5 \times 10^{-4}$, $\eta = 9 \times 10^{-4}$, $\Omega = 5.1716$, $p_0 = 1.0$, $E_0^x = 0.0$, and $E_0^y = 0.02$.

the following simple model with only two coupled modes with energies ω_k and ω_{-k}:

$$\mathcal{H}_{\text{toy}} = \omega_k \hat{a}_k^\dagger \hat{a}_k + \omega_{-k} \hat{a}_{-k}^\dagger \hat{a}_{-k} + 2\epsilon \cos(\Omega t)(\hat{a}_k^\dagger \hat{a}_{-k}^\dagger + \hat{a}_k \hat{a}_{-k}). \tag{8}$$

It can be shown that the fields in the laboratory frame have the following time dependence (see Appendix D):

$$\alpha_{\pm k}^{\text{lab}} = A_\pm(t) e^{\mp i \frac{(\omega_k - \omega_{-k})t}{2}} e^{-i\frac{\Omega}{2}t}, \tag{9}$$

where $A_\pm(t)$ is amplitude modulation due to amplification which becomes time independent in the steady state. From this equation, we can conclude the oscillation frequency due to parametric amplification is half of the driving field only when the coupled state which is amplified has equal energies $\omega_k = \omega_{-k}$; otherwise, the frequency of oscillation is different. Moreover, when effects of oscillation from many coupled oscillators with $\omega_k \neq \omega_{-k}$ are superimposed as in Eq. (6), then the resultant oscillation will be chaotic as in Fig. 3(b).

IV. STABILITY OF THE TIME CRYSTAL

Discrete time crystals of the amplified edge magnons are stable unless bulk eigenmodes with a significant overlap with the edge modes are amplified. The choice of the kagome ferromagnet is preferable because the energy spectrum around the edge state is asymmetrical [see Fig. 2(b)], resulting in suppression of the bulk magnon amplification (see Appendix E, where a comparison with the honeycomb ferromagnet is provided). However, edge magnon scattering can excite other bulk magnon eigenmodes and contribute to the oscillation of spin according to Eq. (6), which may become the reason for instability of the time crystal.

The Hamiltonian $\mathcal{H}_0$ does not contain any magnon nonconserving terms, but such terms may arise in the presence of spin anisotropy in many real quantum magnets. We have calculated the bulk band structure and momentum resolved two-magnon

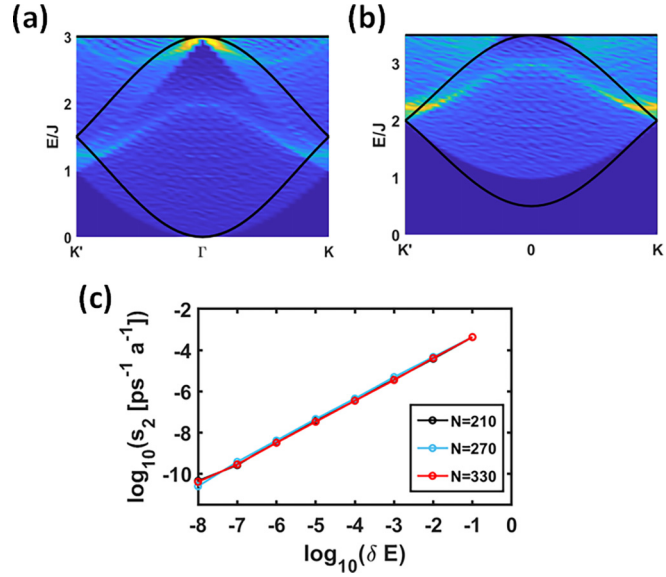

FIG. 4. Two magnon density of states (bluish-yellow color map) and band structure (black line) for (a) zero magnetic field and (b) finite magnetic field $B_z = JS$. With increasing magnetic field, the overlap between two magnon continuum with the band structure decreases, signifying fewer magnon nonconserving scattering. (c) The two-magnon scattering rate as a function of band broadening for different system widths. The scattering rate is $s_2 \leqslant 10\ \text{ns}^{-1}a^{-1}$ for an ideal band broadening $\delta E \leqslant 10^{-2}JS$, indicating a low scattering rate compared with ideal magnon lifetime $\tau_{\text{life}} \leqslant 1$ ns. Thus secondary amplification of bulk magnon is negligible.

density of states

$$D_{\mathbf{k}}(\omega) = \frac{1}{N} \sum_{n,n',\mathbf{\Delta}} \delta(\omega - \omega_{n,\mathbf{\Delta}} - \omega_{n',\mathbf{k}-\mathbf{\Delta}}) \tag{10}$$

for a system with a toroidal boundary condition [Figs. 4(a) and 4(b)]. When the energy of an eigenstate matches that of the two magnon continuum, it can decay into two magnons with lower energies. The two magnon continuum energy scales as twice the negative of Zeeman term ($2B_zS$) of a longitudinal magnetic field B_z, while that of the magnon bands scale as B_zS. Hence for magnetic fields $B_zS > E_{\text{edge}}$ the edge states are energetically separated from the two-magnon continuum and cannot decay via this channel. At even higher fields, $B_z > 6J$, the two-magnon continuum gets separated in energy from the magnon band structure, implying that two edge magnons cannot combine and produce a higher energy magnon. As the magnetic field increases, the higher order magnon nonconserving processes will disappear faster than the two magnon decay processes. Thus an external magnetic field can suppress the magnon nonconserving scattering in the system.

Magnon conserving scattering processes cannot be eliminated by an external field and are always present in any spin Hamiltonian. We calculated the scattering rate of magnons due to two-magnon scattering (quartic terms of magnon Hamiltonian) using Fermi's golden rule,

$$s_2 = \frac{2\pi}{\hbar} \sum_f \sum_i |\langle f||\mathcal{H}_{0,\text{int}}^{(4)}||i\rangle|^2 \delta(E_f - E_i), \tag{11}$$

where $|f\rangle$ and E_f ($|i\rangle$ and E_i) denote the state and energy of the final (initial) state, respectively. $\mathcal{H}^{(4)}_{0,\text{int}}$ is the quartic term of the magnon Hamiltonian which is obtained by Taylor series expansion of the Holstein-Primakoff transformation,

$$\mathcal{H}^{(4)}_{0,\text{int}} = -\frac{J\hbar^2}{4}\sum_{\langle ij\rangle}[4\hat{a}_i^\dagger\hat{a}_j^\dagger\hat{a}_i\hat{a}_j + \hat{a}_j^\dagger\hat{a}_j^\dagger\hat{a}_i\hat{a}_j + \hat{a}_i^\dagger\hat{a}_j^\dagger\hat{a}_i\hat{a}_i + \hat{a}_i^\dagger\hat{a}_j^\dagger\hat{a}_j\hat{a}_j + \hat{a}_i^\dagger\hat{a}_i^\dagger\hat{a}_i\hat{a}_j], \quad (12)$$

where higher order terms of the expansion are neglected which have amplitudes of order $O(\frac{1}{S^n})$, $n \in \mathbb{I} \geqslant 1$. For simplicity, we have restricted our calculation to the upper-edge states and considered only the scattering from the points $k = \pm\pi$ and $k = \pm\pi \pm \delta k$ (where $\delta k = 0.0628$). To numerically calculate the scattering rate s_2, we have considered a finite width of energy levels δE, which physically implies band broadening. The scattering rate as a function of band broadening is plotted in a logarithmic scale in Fig. 4(c) for different system sizes. It is observed that the scattering rate decreases rapidly as the band broadening decreases. The band broadening results from magnon interactions and the only way to control the bandwidth is by controlling the density of the amplified magnons. This is achieved by working at low temperature and low EM field intensity. Even if the scattering rate is high, as long as the lifetime of magnons at the scattered state is small the behavior of the system is governed by only the selectively amplified edge state magnons [12]. For example, the band broadening of an ideal magnon band structure $\delta E \leqslant 10^{-2}JS$, corresponding to scattering rate $s_2 \leqslant 10^{-4}$ ps$^{-1}a^{-1} = 10$ ns$^{-1}a^{-1}$, can be interpreted as maximum one edge magnon is scattered to the bulk magnon every 10 ns, so secondary amplification of bulk magnon is not possible since their lifetimes are usually less than 1 ns. Even in the worst case scenario of large band broadening, a small density of amplified edge state magnons is preferable to create a stable time crystal. These conditions also help minimize magnon decay due to magnon-phonon scattering. Finally, edge imperfections cause broadening of the edge states and reduce the yield of coherent magnons [84,85].

The reduced scattering is a consequence of the topological protection of the edge state. The presence of chiral symmetry induces a flat edge mode at zero energy due to finite π-Berry phase. Absence of chiral symmetry can result in a dispersive edge state at nonzero energy in the presence of a quantized nonzero π-Berry phase [75,76]. Interestingly, the π-Berry phase protected topological edge states are robust against impurities with or without chiral symmetry [76], providing additional stability to the time crystalline behavior.

V. EXPERIMENTAL REALIZATION

The edge-magnon time crystals can be observed using direct spatial and temporal imaging of spin-wave dynamics via multiple recently developed techniques, such as Kerr microscopy [86,87], Brillouin light scattering spectroscopy (BLS) [88–90], and time resolved scanning transmission x-ray microscopy (TR-STXM) [13,91–101]. BLS is useful to detect magnons at a fixed frequency and wave vector [102–107] and has recently been used to detect the space-time crystal in the ferromagnetic insulator YIG [12]. Additionally, theoretically proposed spin Hall noise spectroscopy is a promising technique to detect the presence of edge magnons at a given frequency [108,109]. The TR-STXM, in particular, is promising for directly imaging spin dynamics at the edge due to its high accuracy in detecting magnon dynamics with a spatial and temporal resolution of 20 nm and 50 ps, respectively [13,91–93]. Recently, this method has been used to observe the dynamics of the space-time crystal of bulk magnons in permalloy strips [13].

The required estimated electric field amplitude to amplify topological edge magnons is in between 10^6 and 10^{12} V/m, depending on damping of edge magnons—weaker damping requires lower intensity (see Appendix F).

We propose the spin-$\frac{1}{2}$ kagome ferromagnets haydeeite [110] and Cu(1,3-bdc) [111] as possible hosts of the discrete time crystals of edge magnons as discussed in this work. While the Haydeeite has experimental evidence for the absence of DMI [110], the Cu(1,3-bdc) contains out-of-plane DMI that does not break any effective time reversal symmetry [77] for the ferromagnetic ground state with in-plane magnetization [112]. The period of oscillations for the materials haydeeite and Cu(1,3-bdc) is calculated to be 0.05 ps and 0.25 ps, respectively, which are estimated using experimentally determined Heisenberg exchange interactions [110,111]. Thus these quantum magnets are perfect candidates for realizing discrete time crystals of edge magnons.

ACKNOWLEDGMENTS

B.Y. would like to acknowledge the support from the Singapore National Research Foundation (NRF) under NRF Fellowship Award No. NRF-NRFF12-2020-0005 and a Nanyang Technological University start-up grant (NTU-SUG). D.B. and P.S. acknowledge financial support from the Ministry of Education, Singapore through Grant No. MOE2019-T2-2-119.

APPENDIX A: POLARIZATION OPERATOR

The form of the polarization operator depends on the lattice symmetries and is independent of the magnetic ground state. However, for the estimation of the coefficient of the polarization operator, one requires a more fundamental electronic model. There are various possible electronic models for the spin exchange interactions in different materials. One of the most simplistic electronic models is the Hubbard model. Despite its limitations, the simplistic Hubbard model is used to give an estimation of the coefficients of the polarization operator. The Hubbard model is given by

$$\mathcal{H}_{\text{Hubbard}} = -\sum_{ij}\Bigg[(\hat{c}^\dagger_{i\uparrow} \quad \hat{c}^\dagger_{i\downarrow})[t\mathbb{I}\cos(\theta) + it\boldsymbol{n}\cdot\boldsymbol{\sigma}\sin(\theta)]\begin{pmatrix}\hat{c}_{j\uparrow}\\ \hat{c}_{j\downarrow}\end{pmatrix} + \text{H.c.}\Bigg] + U\sum_i \hat{n}_{i\uparrow}\hat{n}_{j\downarrow}, \quad (A1)$$

where $t\cos(\theta)$ and $it\boldsymbol{n}\sin(\theta)$ ($\boldsymbol{n}$ is a unit vector) are the real and complex hopping amplitudes of electrons on nearest neighbor bonds, respectively. U is the on-site Coulomb repulsion. The polarization operator corresponding to the Hubbard model is [78]

$$\mathbf{P}_{ij} \approx \boldsymbol{p}_{0,ij}(\mathbf{S}_i \cdot \mathbf{Q}_{ij})(\mathbf{S}_j \cdot \mathbf{Q}_{ij}), \tag{A2}$$

where the $\mathbf{p}_{0,ij}$ and $\boldsymbol{Q}_{ij}$ are given by

$$\begin{aligned} \boldsymbol{p}_{0,ij} &= -16\theta^2 ea\frac{t^3}{U^3}(\boldsymbol{e}_{jk} - \boldsymbol{e}_{ki}) = p_0(\boldsymbol{e}_{jk} - \boldsymbol{e}_{ki}), \\ \boldsymbol{Q}_{ij} &= \boldsymbol{n} - n^z\hat{z}, \end{aligned} \tag{A3}$$

where e and a are the electron charge and lattice constant, respectively. $\boldsymbol{e}_{jk}$ is a vector on nearest neighbor bonds from site j to site k. The sites i, j, and k are the sites on the same triangle of the kagome lattice. The polarization terms other than the terms in Eq. (A2) are not important for this study because in the diagonal basis in the rotating frame those terms are time dependent and so those terms are dropped in rotating wave approximation in Eq. (4). Thus the polarization operator is proportional to $\frac{t^3}{U^3}$.

APPENDIX B: DERIVATION OF EQUATION OF MOTION

The Hamiltonian describing a kagome ferromagnet on a cylindrical geometry, coupled to an external EM field, is given by

$$\begin{aligned} \mathcal{H} =& \frac{1}{2}\sum_k (\Psi_k^\dagger \quad \Psi_{-k}) \begin{pmatrix} H_0(k) & O_{N\times N} \\ O_{N\times N} & H_0(-k)^T \end{pmatrix} \begin{pmatrix} \Psi_k \\ \Psi_{-k}^\dagger \end{pmatrix} \\ &+ \frac{1}{2}\cos(\Omega t)\sum_k (\Psi_k^\dagger \quad \Psi_{-k}) \begin{pmatrix} [H_c]_{11} & [H_c]_{12} \\ [H_c]_{21} & [H_c]_{22} \end{pmatrix} \begin{pmatrix} \Psi_k \\ \Psi_{-k}^\dagger \end{pmatrix}. \end{aligned} \tag{B1}$$

N is the number of sites along the width of the ribbon [see Fig. 2(a) in main text] and $\Psi_k = (\hat{a}_{1,k}, \hat{a}_{2,k}, \ldots, \hat{a}_{N,k})^T$. $O_{N\times N}$ is a null matrix. The first and second matrices are derived from the unperturbed Hamiltonian Eq. (1) and coupling Hamiltonian Eq. (2) in the main text, respectively. The Hamiltonian $\mathcal{H}$ is first represented in the diagonal basis $\tilde{\Psi}_k = U_1(k)\Psi_k$, $\tilde{\Psi}_{-k}^\dagger = U_2(k)\Psi_{-k}^\dagger$ of matrices $H_0(k)$, $H_0(-k)^T$. This is followed by transforming the system from the laboratory frame to rotating frame by using the unitary operator $U(t) = \exp\frac{i\omega t}{2}\sum_k \tilde{\Psi}_k^\dagger\tilde{\Psi}_k$,

$$\mathcal{H}' = U(t)\mathcal{H}U(t)^\dagger + i\hbar\dot{U}(t)U(t)^\dagger. \tag{B2}$$

Afterwards, by neglecting the time-dependent terms, we get the following effective Hamiltonian:

$$\mathcal{H}_{\text{eff}} = \frac{1}{2}\sum_k (\tilde{\Psi}_k^\dagger \quad \tilde{\Psi}_{-k})) \begin{pmatrix} \epsilon_k - \frac{\Omega}{2} & \frac{[\tilde{H}_c]_{12}}{2} \\ \frac{[\tilde{H}_c]_{21}}{2} & \epsilon_{-k} - \frac{\Omega}{2} \end{pmatrix} \begin{pmatrix} \tilde{\Psi}_k \\ \tilde{\Psi}_{-k}^\dagger \end{pmatrix}, \tag{B3}$$

where ϵ_k and ϵ_{-k} are the diagonal matrices of eigenvalues of matrices $H_0(k)$ and $H_0(-k)^T$, respectively. The matrix $\tilde{H}_{12} = U_1 H_{12} U_2^\dagger$ is the coupling matrix in the diagonal basis. Only the off-diagonal terms $[\tilde{H}]_{12}$ and $[\tilde{H}]_{21}$ of the coupling Hamiltonian appear in $\mathcal{H}_{\text{eff}}$ due to the rotating wave approximation. The equation of motion of field $\langle\tilde{\Psi}_k\rangle = \tilde{\alpha}_k = (\langle\hat{\tilde{a}}_{1,k}\rangle, \langle\hat{\tilde{a}}_{2,k}\rangle, \ldots, \langle\hat{\tilde{a}}_{N,k}\rangle)^T$ is given by

$$\frac{d}{dt}\begin{pmatrix} \tilde{\alpha}_k^* \\ \tilde{\alpha}_{-k} \end{pmatrix} = \mathrm{i}\begin{pmatrix} \tilde{\epsilon}_k - \mathrm{i}\frac{\gamma\mathbb{I}+\eta|\alpha_k|^2}{2} & \frac{[\tilde{H}_c]_{12}}{2} \\ -\frac{[\tilde{H}_c]_{21}}{2} & -\tilde{\epsilon}_{-k} - \mathrm{i}\frac{\gamma\mathbb{I}+\eta|\alpha_k|^2}{2} \end{pmatrix}\begin{pmatrix} \tilde{\alpha}_k^* \\ \tilde{\alpha}_{-k} \end{pmatrix}, \tag{B4}$$

where $\hat{\tilde{a}}_{n,k}$ is the magnon annihilation operator of nth band at k point; $\tilde{\epsilon}_k$ is a diagonal matrix with elements $\epsilon_{n,k} - \frac{\Omega}{2}$, where $\epsilon_{n,k}$ is the energy eigenvalue; γ and η are phenomenological linear and nonlinear damping constants; $\mathbb{I}$ is identity matrix and $|\alpha_k|^2$ is diagonal matrix with entries $|\langle\hat{\tilde{a}}_{n,k}\rangle|^2$.

APPENDIX C: EQUILIBRATION OF SPIN OSCILLATION

In this section, we show that the oscillation at different k points equilibrates at different times [see Figs. 5(a) and 5(b)] resulting in a transient modulation of amplitude before reaching the steady state as in Fig. 2(d) in the main text. The figure also shows that the amplitude of oscillation decreases rapidly away from $k = \pi$.

APPENDIX D: TOY MODEL FOR ANALYTICAL CALCULATION OF DYNAMICS

In the main text we showed that the time crystal is not stable in the absence of effective time reversal symmetry. The reason behind this chaotic oscillation can be understood from the following simple model with only two coupled modes with energies ω_k and ω_{-k}:

$$\mathcal{H} = \omega_k\hat{a}_k^\dagger\hat{a}_k + \omega_{-k}\hat{a}_{-k}^\dagger\hat{a}_{-k} + 2\epsilon\cos(\Omega t)(\hat{a}_k^\dagger\hat{a}_{-k}^\dagger + \hat{a}_k\hat{a}_{-k}). \tag{D1}$$

Next we rotate the basis states with the unitary operator $U = e^{i\Omega(\hat{n}_k+\hat{n}_{-k})t}$, where $\hat{n}_k = \hat{a}_k^\dagger\hat{a}_k$. The Hamiltonian in rotating frame is

$$\begin{aligned} \mathcal{H}' &= U(t)\mathcal{H}U^\dagger(t) + i\hbar\dot{U}(t)U^\dagger(t) \\ &= \tilde{\omega}_k\hat{a}_k^\dagger\hat{a}_k + \tilde{\omega}_{-k}\hat{a}_{-k}^\dagger\hat{a}_{-k} + \epsilon(e^{2i\Omega t}+1)\hat{a}_k^\dagger\hat{a}_{-k}^\dagger \\ &\quad + \epsilon(1+e^{-2i\Omega t})\hat{a}_k\hat{a}_{-k}, \end{aligned} \tag{D2}$$

where $\tilde{\omega}_k = \omega_k - \Omega/2$. Neglecting fast rotations (terms with $e^{\pm 2i\Omega t}$), the effective Hamiltonian in rotating wave approximation becomes

$$\mathcal{H}_{\text{eff}} = \tilde{\omega}_k\hat{a}_k^\dagger\hat{a}_k + \tilde{\omega}_{-k}\hat{a}_{-k}^\dagger\hat{a}_{-k} + \epsilon\hat{a}_k^\dagger\hat{a}_{-k}^\dagger + \epsilon\hat{a}_k\hat{a}_{-k}. \tag{D3}$$

By defining the field $\alpha_k = \langle\hat{a}_k\rangle$ and using the equation of motion $i\frac{d}{dt}\langle\hat{O}\rangle = \langle[\hat{O}, \hat{H}_{\text{eff}}]\rangle$, we get the following coupled differential equation:

$$i\frac{d}{dt}\begin{pmatrix} \alpha_k \\ \alpha_{-k}^* \end{pmatrix} = \begin{pmatrix} \tilde{\omega}_k - i\frac{\gamma}{2} & \epsilon \\ -\epsilon & -\tilde{\omega}_{-k} - i\frac{\gamma}{2} \end{pmatrix}\begin{pmatrix} \alpha_k \\ \alpha_{-k}^* \end{pmatrix}, \tag{D4}$$

where the phenomenological damping γ is added. The coupled differential equation can be transformed into

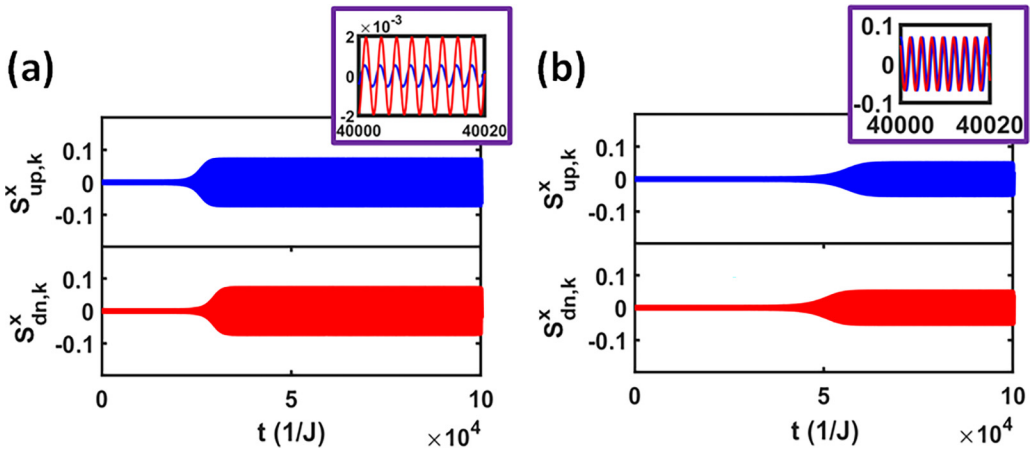

FIG. 5. Oscillation of spin component S^x at a site at upper edge (blue plot) and lower edge (red plot) are calculated (d) at $k = \pi$ and (e) at $k = 3.1793$ in Brillouin zone for a system with $N_y = 91$. Insets show the magnified figures of the corresponding figures within a particular time limit. The parameters used for all the plots are $J = 1.0$, $B_z \to 0^+$, $\gamma = 5 \times 10^{-4}$, $\eta = 9 \times 10^{-4}$, $\Omega = 5.1716$, $p_0 = 1.0$, $E_0^x = 0.0$, and $E_0^y = 0.002$. The figure shows that the different k points arrive at steady state at a different time and the amplitude of oscillation decreases rapidly away from $k = \pi$.

the following second order differential equation:

$$\frac{d^2\alpha_k}{dt^2} - (\tilde{\omega}_k - \tilde{\omega}_{-k} - i\gamma)\frac{d\alpha_k}{dt} + \left[\epsilon^2 - \left(\tilde{\omega}_k - i\frac{\gamma}{2}\right)\left(\tilde{\omega}_{-k} + i\frac{\gamma}{2}\right)\right] = 0. \tag{D5}$$

Now using the ansatz $\alpha_k = A_1 e^{-i\omega t}$ we get a quadratic equation in ω, the solution of which is given by

$$\omega = \frac{\omega_k - \omega_{-k}}{2} - i\frac{\gamma}{2} \pm i\sqrt{\epsilon - \frac{(\tilde{\omega}_k + \tilde{\omega}_{-k})^2}{4}}. \tag{D6}$$

The solution with positive sign is the only physical solution, because in the limit $\epsilon \to 0$ the frequency should be $\omega \to \omega_k$. Thus the solution for the field

$$\alpha_k = A_+ e^{-i\frac{(\omega_k - \omega_k)t}{2}} e^{-\frac{\gamma t}{2}} e^{\sqrt{\epsilon - \frac{(\tilde{\omega}_k + \tilde{\omega}_{-k})}{4}}t}. \tag{D7}$$

Thus the condition for amplification is given by

$$\sqrt{\epsilon - \frac{(\tilde{\omega}_k + \tilde{\omega}_{-k})}{4}} > \frac{\gamma}{2}. \tag{D8}$$

From now on, we focus on the oscillatory part of the solution, by taking the exponential decay or amplification into the amplitude,

$$\alpha_k = A_+(t) e^{-i\frac{(\omega_k - \omega_{-k})t}{2}}. \tag{D9}$$

From Eq. (D4), we get $\alpha^*_{-k} = A_-(t) e^{-i\frac{(\omega_k - \omega_{-k})t}{2}}$, and thus we have

$$\alpha_{-k} = A_-(t) e^{i\frac{(\omega_k - \omega_{-k})t}{2}}. \tag{D10}$$

It can be shown that the relation between the fields in laboratory and rotating frame is given by $\alpha^{\text{lab}}_{\pm k} = e^{-i\frac{\Omega}{2}t}\alpha_{\pm k}$; thus the fields in laboratory frame are given by

$$\alpha^{\text{lab}}_{\pm k} = A_\pm(t) e^{\mp i\frac{(\omega_k - \omega_{-k})t}{2}} e^{-i\frac{\Omega}{2}t}. \tag{D11}$$

From this equation, we can conclude the oscillation frequency due to parametric amplification is half of the driving field only when the coupled state which is amplified has equal energies $\omega_k = \omega_{-k}$; otherwise, the frequency of oscillation is different. Moreover, when effects of oscillation from many coupled oscillators with $\omega_k \neq \omega_{-k}$ are superimposed as in Eq. (6) in the main text, then the resultant oscillation will be chaotic, which is visible in Fig. 3(b).

APPENDIX E: COMPARISON BETWEEN KAGOME LATTICE AND HONEYCOMB LATTICE

In this section we show that kagome lattice structure is a suitable lattice structure for achieving a magnon time crystal, by comparing the results with the honeycomb lattice. We have studied a similar model in the honeycomb lattice to show the advantage of the kagome lattice structure. The model Hamiltonian we take on the honeycomb lattice is given as

$$\begin{aligned}\mathcal{H} = &-J\sum_{\langle ij\rangle}\hat{\mathbf{S}}_i \cdot \hat{\mathbf{S}}_j + E^x(t)\sum_i K_i^{x,xy}\left[\hat{S}^x_{j,A}\hat{S}^y_{j,A} - \hat{S}^x_{j,B}\hat{S}^y_{j,B}\right] \\ &+ E^y(t)\sum_i \left[K_j^{y,xx}\left(\hat{S}^x_{j,A}\hat{S}^x_{j,A} + \hat{S}^x_{j,B}\hat{S}^x_{j,B}\right)\right. \\ &\left. + K_j^{y,yy}\left(\hat{S}^y_{j,A}\hat{S}^y_{j,A} + \hat{S}^y_{j,B}\hat{S}^y_{j,B}\right)\right],\end{aligned} \tag{E1}$$

where the polarization terms are considered with respect to the symmetry of the lattice and the terms which do not contribute to the amplification are already discarded (mathematically those terms will be discarded in rotating wave approximation). By diagonalizing the dynamical matrix as discussed in the main text we achieved the band structure as shown in Figs. 6(a) and 6(b) for different polarization. It can be noticed that the electromagnetic field amplifies the bulk magnon bands instead of the edge magnon bands, which is backed up by the results in Figs. 6(c) and 6(d) showing maximum coupling with electromagnetic field occurs with the bulk magnon states.

Whereas the kagome lattice structure is useful for amplification of edge magnons without amplifying the bulk magnons, the reason behind not amplifying the bulk magnons is for

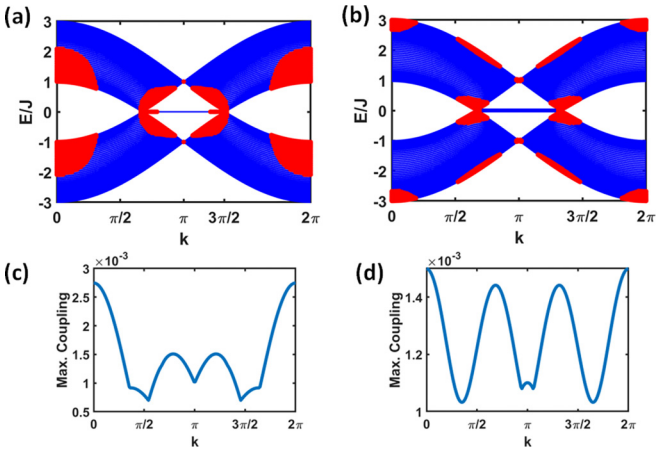

FIG. 6. Magnon band structure is shown in blue, whereas the red dots denote eigenstate with eigenvalues with positive imaginary part for electric fields (a) $E_0^y = 0.015$ and (b) $E_0^x = 0.015$. Maximum of absolute values of matrix elements $[\tilde{H}_c]_{12}$ is plotted as a function of momentum for electric field amplitudes (c) $E_0^y = 0.001$ and (d) $E_0^x = 0.002$. The other parameters used for all the plots are $J = 1.0$, $S = 1$, $B_z \to 0^+$, $\gamma = 2.5 \times 10^{-3}$, $\Omega = 3JS$, and $K^{x,xy} = K^{y,xx} = K^{y,yy} = 1.0$.

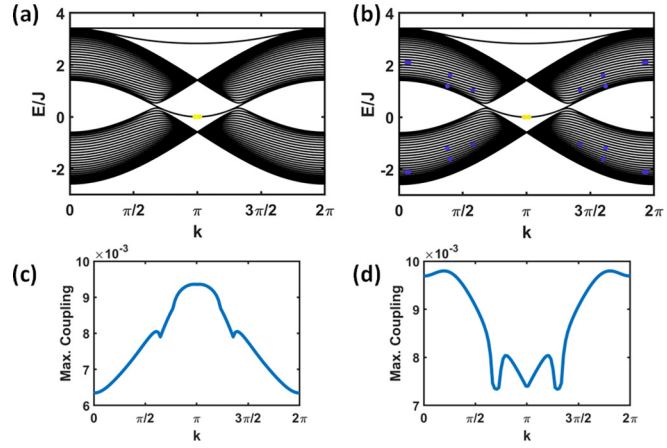

FIG. 7. Magnon band structure is shown in black; the yellow and blue dots denote eigenstate with eigenvalues with positive imaginary part for electric fields (a) $E_0^y = 0.015$ and (b) $E_0^x = 0.015$. Maximum of absolute values of matrix elements $[\tilde{H}_c]_{12}$ is plotted as a function of momentum for electric field amplitudes (c) $E_0^y = 0.015$ and (d) $E_0^x = 0.015$. The other parameters used for all the plots are $J = 1.0$, $D = 0.00$, $B_z \to 0^+$, $\gamma = 5 \times 10^{-4}$, $\Omega = 5.1716$, and $p_0 = 1.0$.

making the system more stable. Figures 7(a) and 7(b) show that the magnon amplification in the kagome lattice is confined to the edge states only. Moreover, choice of polarization of electromagnetic field should be in the y direction to specifically amplify the edge magnons. Figures 7(a) and 7(b) show the imaginary parts of bulk magnon modes zero and nonzero for y-polarized and x-polarized electromagnetic field. The reason for this discrepancy is due to the difference in coupling terms as shown in Figs. 7(c) and 7(d). The y-polarized EM-field strongly couples with edge magnons, whereas the x-polarized EM field strongly couples with bulk magnons.

APPENDIX F: REQUIRED INTENSITY OF LIGHT AND THE EFFECT OF MAGNETIC FIELD OF ELECTROMAGNETIC WAVE

In this section, we discuss the effect of magnetic field and intensity of light that is required for the amplification procedure. The intensity of light that is required to get amplification is unknown and depends on damping of magnon states. The lifetime of magnons can be 1 μs, 1 ns, 1 ps, etc. Depending on that, the energy-state broadening according to the uncertainty principle would be 10^{-9} eV, 10^{-6} eV, 10^{-3} eV, respectively. Thus the damping parameters should be $\lambda = 10^{-9}$ eV, 10^{-6} eV, 10^{-3} eV, respectively. Now, to have amplification, one is required to have electric field amplitude E_c (V/nm), which should follow the inequality relationship for a system with damping λ (considering the following ideal system parameters, lattice constant $a = 1$ nm, $t/U = 10^{-2}$),

$$\begin{aligned} E_c P &\geqslant \lambda[\text{eV}], \\ E_c a[\text{nm}] e (t/U)^3 &\geqslant \lambda[\text{eV}] \left[\text{where } P \approx a\, e \frac{t^3}{U^3}\right], \\ E_c \times 10^{-6} &\geqslant \lambda\ \text{V/nm}, \\ E_c &\geqslant 10^6 \lambda\ \text{V/nm}, \\ E_c &\geqslant 10^{15} \lambda\ \text{V/m}. \end{aligned} \tag{F1}$$

Thus the electric field required for the amplification should be 10^6 V/m, 10^9 V/m, 10^{12} V/m respectively. Based on the relation $B = E/c$, the magnetic field amplitude should be $B = 0.01$ T, 1 T, 1000 T, respectively. The magnetic fields 0.01 T and 1 T are still very negligible for a magnetic insulator, because the Heisenberg exchange interaction is 1 meV, whereas the energy equivalent to 1 T is $\mu_B B = 0.01$ meV.

[1] F. Wilczek, Quantum Time Crystals, Phys. Rev. Lett. **109**, 160401 (2012).

[2] P. Bruno, Impossibility of Spontaneously Rotating Time Crystals: A No-Go Theorem, Phys. Rev. Lett. **111**, 070402 (2013).

[3] P. Bruno, Comment on "Quantum Time Crystals", Phys. Rev. Lett. **110**, 118901 (2013).

[4] P. Nozières, Time crystals: Can diamagnetic currents drive a charge density wave into rotation? Europhys. Lett. **103**, 57008 (2013).

[5] H. Watanabe and M. Oshikawa, Absence of Quantum Time Crystals, Phys. Rev. Lett. **114**, 251603 (2015).

[6] H. Watanabe, M. Oshikawa, and T. Koma, Proof of the absence of long-range temporal orders in Gibbs states, J. Stat. Phys. **178**, 926 (2020).

[7] N. V. Prokof'ev and B. V. Svistunov, Algebraic time crystallization in a two-dimensional superfluid, JETP **127**, 860 (2018).

[8] N. Prokof'ev and B. Svistunov, Space- and time-crystallization effects in multicomponent superfluids, Phys. Rev. B **101**, 020505(R) (2020).

[9] G. E. Volovik, On the broken time translation symmetry in macroscopic systems: Precessing states and off-diagonal long-range order, JETP Lett. **98**, 491 (2013).

[10] F. Wilczek, Superfluidity and Space-Time Translation Symmetry Breaking, Phys. Rev. Lett. **111**, 250402 (2013).

[11] D. V. Else, B. Bauer, and C. Nayak, Prethermal Phases of Matter Protected by Time-Translation Symmetry, Phys. Rev. X **7**, 011026 (2017).

[12] A. J. E. Kreil, H. Y. Musiienko-Shmarova, S. Eggert, A. A. Serga, B. Hillebrands, D. A. Bozhko, A. Pomyalov, and V. S. L'vov, Tunable space-time crystal in room-temperature magnetodielectrics, Phys. Rev. B **100**, 020406(R) (2019).

[13] N. Träger, P. Gruszecki, F. Lisiecki, F. Groß, J. Förster, M. Weigand, H. Głowiński, P. Kuświk, J. Dubowik, G. Schütz, M. Krawczyk, and J. Gräfe, Real-Space Observation of Magnon Interaction with Driven Space-Time Crystals, Phys. Rev. Lett. **126**, 057201 (2021).

[14] K. Sacha, Modeling spontaneous breaking of time-translation symmetry, Phys. Rev. A **91**, 033617 (2015).

[15] J. Smits, L. Liao, H. T. C. Stoof, and P. van der Straten, Observation of a Space-Time Crystal in a Superfluid Quantum Gas, Phys. Rev. Lett. **121**, 185301 (2018).

[16] L. Liao, J. Smits, P. van der Straten, and H. T. C. Stoof, Dynamics of a space-time crystal in an atomic Bose-Einstein condensate, Phys. Rev. A **99**, 013625 (2019).

[17] X. Mi, M. Ippoliti, C. Quintana, A. Greene, Z. Chen, J. Gross, F. Arute, K. Arya, J. Atalaya, R. Babbush *et al.*, Time-crystalline eigenstate order on a quantum processor, Nature (London) **601**, 531 (2022).

[18] A. Kyprianidis, F. Machado, W. Morong, P. Becker, K. S. Collins, D. V. Else, L. Feng, P. W. Hess, C. Nayak, G. Pagano, N. Y. Yao, and C. Monroe, Observation of a prethermal discrete time crystal, Science **372**, 1192 (2021).

[19] J. Randall, C. E. Bradley, F. V. van der Gronden, A. Galicia, M. H. Abobeih, M. Markham, D. J. Twitchen, F. Machado, N. Y. Yao, and T. H. Taminiau, Many-body–localized discrete time crystal with a programmable spin-based quantum simulator, Science **374**, 1474 (2021).

[20] P. Kongkhambut, J. Skulte, L. Mathey, J. G. Cosme, A. Hemmerich, and H. Keßler, Observation of a continuous time crystal, Science **377**, 670 (2022).

[21] M. Krishna, P. Solanki, M. Hajdušek, and S. Vinjanampathy, Measurement-Induced Continuous Time Crystals, Phys. Rev. Lett. **130**, 150401 (2023).

[22] J. R. M. de Nova and F. Sols, Continuous-time crystal from a spontaneous many-body Floquet state, Phys. Rev. A **105**, 043302 (2022).

[23] T. Liu, J.-Y. Ou, K. F. MacDonald, and N. I. Zheludev, Photonic metamaterial analogue of a continuous time crystal, Nat. Phys. **19**, 986 (2023).

[24] D. V. Else, B. Bauer, and C. Nayak, Floquet Time Crystals, Phys. Rev. Lett. **117**, 090402 (2016).

[25] D. V. Else, C. Monroe, C. Nayak, and N. Y. Yao, Discrete time crystals, Annu. Rev. Condens. Matter Phys. **11**, 467 (2020).

[26] N. Y. Yao, A. C. Potter, I.-D. Potirniche, and A. Vishwanath, Discrete Time Crystals: Rigidity, Criticality, and Realizations, Phys. Rev. Lett. **118**, 030401 (2017).

[27] S. Choi, J. Choi, R. Landig, G. Kucsko, H. Zhou, J. Isoya, F. Jelezko, S. Onoda, H. Sumiya, V. Khemani *et al.*, Observation of discrete time-crystalline order in a disordered dipolar many-body system, Nature (London) **543**, 221 (2017).

[28] S. Pal, N. Nishad, T. S. Mahesh, and G. J. Sreejith, Temporal Order in Periodically Driven Spins in Star-Shaped Clusters, Phys. Rev. Lett. **120**, 180602 (2018).

[29] J. Rovny, R. L. Blum, and S. E. Barrett, ^{31}P-NMR study of discrete time-crystalline signatures in an ordered crystal of ammonium dihydrogen phosphate, Phys. Rev. B **97**, 184301 (2018).

[30] J. Rovny, R. L. Blum, and S. E. Barrett, Observation of Discrete-Time-Crystal Signatures in an Ordered Dipolar Many-Body System, Phys. Rev. Lett. **120**, 180603 (2018).

[31] J. Zhang, P. W. Hess, A. Kyprianidis, P. Becker, A. Lee, J. Smith, G. Pagano, I.-D. Potirniche, A. C. Potter, A. Vishwanath *et al.*, Observation of a discrete time crystal, Nature (London) **543**, 217 (2017).

[32] P. Matus and K. Sacha, Fractional time crystals, Phys. Rev. A **99**, 033626 (2019).

[33] A. Pizzi, J. Knolle, and A. Nunnenkamp, Higher-order and fractional discrete time crystals in clean long-range interacting systems, Nat. Commun. **12**, 2341 (2021).

[34] K. Giergiel, A. Kuroś, and K. Sacha, Discrete time quasicrystals, Phys. Rev. B **99**, 220303(R) (2019).

[35] M. I. Dykman, Coherent multiple-period states of periodically modulated qubits, Phys. Rev. A **100**, 042101 (2019).

[36] F. Flicker, Time quasilattices in dissipative dynamical systems, SciPost Phys. **5**, 001 (2018).

[37] Y. Huang, T. Li, and Z.-q. Yin, Symmetry-breaking dynamics of the finite-size Lipkin-Meshkov-Glick model near ground state, Phys. Rev. A **97**, 012115 (2018).

[38] D. J. Luitz, A. Lazarides, and Y. Bar Lev, Periodic and quasiperiodic revivals in periodically driven interacting quantum systems, Phys. Rev. B **97**, 020303(R) (2018).

[39] Y. Peng and G. Refael, Time-quasiperiodic topological superconductors with Majorana multiplexing, Phys. Rev. B **98**, 220509(R) (2018).

[40] F. M. Gambetta, F. Carollo, M. Marcuzzi, J. P. Garrahan, and I. Lesanovsky, Discrete Time Crystals in the Absence of Manifest Symmetries or Disorder in Open Quantum Systems, Phys. Rev. Lett. **122**, 015701 (2019).

[41] Z. Gong, R. Hamazaki, and M. Ueda, Discrete Time-Crystalline Order in Cavity and Circuit QED Systems, Phys. Rev. Lett. **120**, 040404 (2018).

[42] A. Lazarides, S. Roy, F. Piazza, and R. Moessner, Time crystallinity in dissipative Floquet systems, Phys. Rev. Res. **2**, 022002(R) (2020).

[43] B. Zhu, J. Marino, N. Y Yao, M. D. Lukin, and E. A. Demler, Dicke time crystals in driven-dissipative quantum many-body systems, New J. Phys. **21**, 073028 (2019).

[44] J. O'Sullivan, O. Lunt, C. W. Zollitsch, M. L. W. Thewalt, J. J. L. Morton, and A. Pal, Signatures of discrete time crystalline order in dissipative spin ensembles, New J. Phys. **22**, 085001 (2020).

[45] N. del Ser, L. Heinen, and A. Rosch, Archimedean screw in driven chiral magnets, SciPost Phys. **11**, 009 (2021).

[46] H. Keßler, P. Kongkhambut, C. Georges, L. Mathey, J. G. Cosme, and A. Hemmerich, Observation of a Dissipative Time Crystal, Phys. Rev. Lett. **127**, 043602 (2021).

[47] Y. Peng, Topological Space-Time Crystal, Phys. Rev. Lett. **128**, 186802 (2022).

[48] K. Giergiel, A. Dauphin, M. Lewenstein, J. Zakrzewski, and K. Sacha, Topological time crystals, New J. Phys. **21**, 052003 (2019).

[49] M. Saba, C. Ciuti, J. Bloch, V. Thierry-Mieg, R. André, L. S. Dang, S. Kundermann, A. Mura, G. Bongiovanni, J. Staehli *et al.*, High-temperature ultrafast polariton parametric amplification in semiconductor microcavities, Nature (London) **414**, 731 (2001).

[50] M. Saba, C. Ciuti, S. Kundermann, J. Staehli, B. Deveaud, J. Bloch, V. Thierry-Mieg, R. André, L. S. Dang, A. Mura, and G. Bongiovanni, Polariton parametric amplification in semiconductor microcavities, J. Mod. Opt. **49**, 2437 (2002).

[51] C. Ciuti, P. Schwendimann, and A. Quattropani, Theory of polariton parametric interactions in semiconductor microcavities, Semicond. Sci. Technol. **18**, S279 (2003).

[52] J. Tignon, A. Huynh, P. Roussignol, C. Delalande, R. Ferreira, R. André, R. Romestain, and L. Si Dang, Polariton parametric amplifier coherent dynamics, Phys. E **21**, 820 (2004).

[53] D. Singh, B. Sharma, and M. Singh, Parametric amplification of acoustical phonons in semiconductor magneto-plasmas: Quantum effects, Mater. Today: Proc. **49**, 1383 (2022), .

[54] J. Gahlawat, S. Dahiya, and M. Singh, High gain coefficient parametric amplification of optical phonon mode in magnetized $A^{III}B^{V}$ semiconductor plasmas, Arabian J. Sci. Eng. **46**, 721 (2021).

[55] J. Gahlawat, S. Dahiya and M. Singh, High gain coefficient parametric amplification and dispersion characteristics of optical phonon mode in a semiconductor magnetoplasma, Pramana **95**, 42 (2021).

[56] A. Cartella, T. F. Nova, M. Fechner, R. Merlin, and A. Cavalleri, Parametric amplification of optical phonons, Proc. Natl. Acad. Sci. USA **115**, 12148 (2018).

[57] M. Mayy, G. Zhu, A. D. Webb, H. Ferguson, T. Norris, V. A. Podolskiy, and M. A. Noginov, Toward parametric amplification in plasmonic systems: Second harmonic generation enhanced by surface plasmon polaritons, Opt. Express **22**, 7773 (2014).

[58] F. Lu, T. Li, J. Xu, Z.-D. Xie, L. Li, S. Zhu, and Y. Zhu, Surface plasmon polariton enhanced by optical parametric amplification in nonlinear hybrid waveguide, Opt. Express **19**, 2858 (2011).

[59] X. Gao, J. Zhang, Y. Luo, Q. Ma, G. D. Bai, H. C. Zhang, and T. J. Cui, Reconfigurable parametric amplifications of spoof surface plasmons, Adv. Sci. **8**, 2100795 (2021).

[60] Y. Zhang, Y. V. Kartashov, and A. Ferrando, Interface states in polariton topological insulators, Phys. Rev. A **99**, 053836 (2019).

[61] C. Li, F. Ye, X. Chen, Y. V. Kartashov, A. Ferrando, L. Torner, and D. V. Skryabin, Lieb polariton topological insulators, Phys. Rev. B **97**, 081103(R) (2018).

[62] Y. Zhang, Y. V. Kartashov, Y. Zhang, L. Torner, and D. V. Skryabin, Resonant edge-state switching in polariton topological insulators, Laser Photon. Rev. **12**, 1700348 (2018).

[63] R. G. Gladstone, S. Dev, J. Allen, M. Allen, and G. Shvets, Topological edge states of a long-range surface plasmon polariton at the telecommunication wavelength, Opt. Lett. **47**, 4532 (2022).

[64] W. Liu, Z. Ji, Y. Wang, G. Modi, M. Hwang, B. Zheng, V. J. Sorger, A. Pan, and R. Agarwal, Generation of helical topological exciton-polaritons, Science **370**, 600 (2020).

[65] M. Li, I. Sinev, F. Benimetskiy, T. Ivanova, E. Khestanova, S. Kiriushechkina, A. Vakulenko, S. Guddala, M. Skolnick, V. M. Menon, D. Krizhanovskii, A. Alù, A. Samusev, and A. B. Khanikaev, Experimental observation of topological Z_2 exciton-polaritons in transition metal dichalcogenide monolayers, Nat. Commun. **12**, 4425 (2021).

[66] H. Ren, T. Shah, H. Pfeifer, C. Brendel, V. Peano, F. Marquardt, and O. Painter, Topological phonon transport in an optomechanical system, Nat. Commun. **13**, 3476 (2022).

[67] Y. Liu, Y. Xu, and W. Duan, Berry phase and topological effects of phonons, Natl. Sci. Rev. **5**, 314 (2018).

[68] R. Süsstrunk and S. D. Huber, Classification of topological phonons in linear mechanical metamaterials, Proc. Natl. Acad. Sci. USA **113**, E4767 (2016).

[69] Z.-K. Ding, Y.-J. Zeng, H. Pan, N. Luo, J. Zeng, L.-M. Tang, and K.-Q. Chen, Edge states of topological acoustic phonons in graphene zigzag nanoribbons, Phys. Rev. B **106**, L121401 (2022).

[70] C. W. Ling, M. Xiao, C. T. Chan, S. F. Yu, and K. H. Fung, Topological edge plasmon modes between diatomic chains of plasmonic nanoparticles, Opt. Express **23**, 2021 (2015).

[71] Z. Song, H. Liu, N. Huang, and Z. Wang, Plasmonic topological edge states in ring-structure gate graphene, Appl. Opt. **57**, 8503 (2018).

[72] M. Honari-Latifpour and L. Yousefi, Topological plasmonic edge states in a planar array of metallic nanoparticles, Nanophotonics **8**, 799 (2019).

[73] J. W. You, Z. Lan, and N. C. Panoiu, Four-wave mixing of topological edge plasmons in graphene metasurfaces, Sci. Adv. **6**, eaaz3910 (2020).

[74] H. Schlömer, Z. Jiang, and S. Haas, Plasmons in two-dimensional topological insulators, Phys. Rev. B **103**, 115116 (2021).

[75] P. Delplace, D. Ullmo, and G. Montambaux, Zak phase and the existence of edge states in graphene, Phys. Rev. B **84**, 195452 (2011).

[76] E. Colomés and M. Franz, Antichiral Edge States in a Modified Haldane Nanoribbon, Phys. Rev. Lett. **120**, 086603 (2018).

[77] A. Mook, K. Plekhanov, J. Klinovaja, and D. Loss, Interaction-Stabilized Topological Magnon Insulator in Ferromagnets, Phys. Rev. X **11**, 021061 (2021).

[78] D. Malz, J. Knolle, and A. Nunnenkamp, Topological magnon amplification, Nat. Commun. **10**, 3937 (2019).

[79] A. Bolens, Theory of electronic magnetoelectric coupling in d^5 Mott insulators, Phys. Rev. B **98**, 125135 (2018).

[80] L. N. Bulaevskii, C. D. Batista, M. V. Mostovoy, and D. I. Khomskii, Electronic orbital currents and polarization in Mott insulators, Phys. Rev. B **78**, 024402 (2008).

[81] S. Zhu, Y.-Q. Li, and C. D. Batista, Spin-orbit coupling and electronic charge effects in Mott insulators, Phys. Rev. B **90**, 195107 (2014).

[82] K. V. Kheruntsyan and P. D. Drummond, Quantum correlated twin atomic beams via photodissociation of a molecular Bose-Einstein condensate, Phys. Rev. A **66**, 031602(R) (2002).

[83] K. V. Kheruntsyan, Matter-wave amplification and phase conjugation via stimulated dissociation of a molecular Bose-Einstein condensate, Phys. Rev. A **71**, 053609 (2005).

[84] M. Tanaka, Y. Fujishiro, M. Mogi, Y. Kaneko, T. Yokosawa, N. Kanazawa, S. Minami, T. Koretsune, R. Arita, S. Tarucha, M. Yamamoto, and Y. Tokura, Topological Kagome magnet $Co_3Sn_2S_2$ thin flakes with high electron mobility and large anomalous Hall effect, Nano Lett. **20**, 7476 (2020).

[85] R. Pawlak, X. Liu, S. Ninova, P. D'Astolfo, C. Drechsel, S. Sangtarash, R. Häner, S. Decurtins, H. Sadeghi, C. J. Lambert, U. Aschauer, S.-X. Liu, and E. Meyer, Bottom-up synthesis of nitrogen-doped porous graphene nanoribbons, J. Am. Chem. Soc. **142**, 12568 (2020).

[86] A. Talalaevskij, M. Decker, J. Stigloher, A. Mitra, H. S. Körner, O. Cespedes, C. H. Back, and B. J. Hickey, Magnetic properties of spin waves in thin yttrium iron garnet films, Phys. Rev. B **95**, 064409 (2017).

[87] J. P. Park, P. Eames, D. M. Engebretson, J. Berezovsky, and P. A. Crowell, Spatially Resolved Dynamics of Localized Spin-Wave Modes in Ferromagnetic Wires, Phys. Rev. Lett. **89**, 277201 (2002).

[88] A. A. Serga, A. V. Chumak, and B. Hillebrands, YIG magnonics, J. Phys. D **43**, 264002 (2010).

[89] A. Chumak, V. Vasyuchka, A. Serga, and B. Hillebrands, Magnon spintronics, Nat. Phys. **11**, 453 (2015).

[90] M. Collet, O. Gladii, M. Evelt, V. Bessonov, L. Soumah, P. Bortolotti, S. O. Demokritov, Y. Henry, V. Cros, M. Bailleul, V. E. Demidov, and A. Anane, Spin-wave propagation in ultra-thin YIG based waveguides, Appl. Phys. Lett. **110**, 092408 (2017).

[91] S. Wintz, V. Tiberkevich, M. Weigand, J. Raabe, J. Lindner, A. Erbe, A. N. Slavin, and J. Fassbender, Magnetic vortex cores as tunable spin-wave emitters, Nat. Nanotechnol. **11**, 948 (2016).

[92] J. Gräfe, M. Weigand, B. V. Waeyenberge, A. Gangwar, F. Groß, F. Lisiecki, J. Rychly, H. Stoll, N. Träger, J. Förster, F. Stobiecki, J. Dubowik, J. Klos, M. Krawczyk, C. H. Back, E. J. Goering, and G. Schütz, Visualizing nanoscale spin waves using MAXYMUS, Proc. SPIE **11090**, 1109025 (2019).

[93] J. Förster, S. Wintz, J. Bailey, S. Finizio, E. Josten, C. Dubs, D. A. Bozhko, H. Stoll, G. Dieterle, N. Träger, J. Raabe, A. N. Slavin, M. Weigand, J. Gräfe, and G. Schütz, Nanoscale x-ray imaging of spin dynamics in yttrium iron garnet, J. Appl. Phys. **126**, 173909 (2019).

[94] B. Van Waeyenberge, A. Puzic, H. Stoll, K. W. Chou, T. Tyliszczak, R. Hertel, M. Fähnle, H. Brückl, K. Rott, G. Reiss, I. Neudecker, D. Weiss, C. Back, and G. Schütz, Magnetic vortex core reversal by excitation with short bursts of an alternating field, Nature (London) **444**, 461 (2006).

[95] Y. Acremann, J. P. Strachan, V. Chembrolu, S. D. Andrews, T. Tyliszczak, J. A. Katine, M. J. Carey, B. M. Clemens, H. C. Siegmann, and J. Stöhr, Time-Resolved Imaging of Spin Transfer Switching: Beyond the Macrospin Concept, Phys. Rev. Lett. **96**, 217202 (2006).

[96] Y. Acremann, V. Chembrolu, J. P. Strachan, T. Tyliszczak, and J. Stöhr, Software defined photon counting system for time resolved x-ray experiments, Rev. Sci. Instrum. **78**, 014702 (2007).

[97] M. Weigand, B. Van Waeyenberge, A. Vansteenkiste, M. Curcic, V. Sackmann, H. Stoll, T. Tyliszczak, K. Kaznatcheev, D. Bertwistle, G. Woltersdorf, C. H. Back, and G. Schütz, Vortex Core Switching by Coherent Excitation with Single In-Plane Magnetic Field Pulses, Phys. Rev. Lett. **102**, 077201 (2009).

[98] C. Cheng and W. E. Bailey, Sub-micron mapping of GHz magnetic susceptibility using scanning transmission x-ray microscopy, Appl. Phys. Lett. **101**, 182407 (2012).

[99] D. Nolle, M. Weigand, P. Audehm, E. Goering, U. Wiesemann, C. Wolter, E. Nolle, and G. Schütz, Note: Unique characterization possibilities in the ultra high vacuum scanning transmission x-ray microscope (UHV-STXM) "MAXYMUS" using a rotatable permanent magnetic field up to 0.22 T, Rev. Sci. Instrum. **83**, 046112 (2012).

[100] S. Bonetti, R. Kukreja, Z. Chen, F. Macià, J. M. Hernàndez, A. Eklund, D. Backes, J. Frisch, J. Katine, G. Malm, S. Urazhdin, A. D. Kent, J. Stöhr, H. Ohldag, and H. A. Dürr, Direct observation and imaging of a spin-wave soliton with *p*-like symmetry, Nat. Commun. **6**, 8889 (2015).

[101] S. Bonetti, R. Kukreja, Z. Chen, D. Spoddig, K. Ollefs, C. Schöppner, R. Meckenstock, A. Ney, J. Pinto, R. Houanche, J. Frisch, J. Stöhr, H. A. Dürr, and H. Ohldag, Microwave soft x-ray microscopy for nanoscale magnetization dynamics in the 5–10 GHz frequency range, Rev. Sci. Instrum. **86**, 093703 (2015).

[102] S. O. Demokritov, V. E. Demidov, O. Dzyapko, G. A. Melkov, A. A. Serga, B. Hillebrands, and A. N. Slavin, Bose–Einstein condensation of quasi-equilibrium magnons at room temperature under pumping, Nature (London) **443**, 430 (2006).

[103] V. E. Demidov, S. Urazhdin, R. Liu, B. Divinskiy, A. V. Telegin, and S. O. Demokritov, Excitation of coherent propagating spin waves by pure spin currents, Nat. Commun. **7**, 10446 (2016).

[104] J. Holanda, D. S. Maior, A. Azevedo, and S. M. Rezende, Detecting the phonon spin in magnon–phonon conversion experiments, Nat. Phys. **14**, 500 (2018).

[105] J. Cho, N.-H. Kim, S. Lee, J.-S. Kim, R. Lavrijsen, A. Solignac, Y. Yin, D.-S. Han, N. J. J. van Hoof, H. J. M. Swagten, B. Koopmans, and C.-Y. You, Thickness dependence of the interfacial Dzyaloshinskii–Moriya interaction in inversion symmetry broken systems, Nat. Commun. **6**, 7635 (2015).

[106] M. Balinskiy, F. Kargar, H. Chiang, A. A. Balandin, and A. G. Khitun, Brillouin-Mandelstam spectroscopy of standing spin waves in a ferrite waveguide, AIP Adv. **8**, 056017 (2018).

[107] F. Kargar and A. Balandin, Advances in Brillouin–Mandelstam light-scattering spectroscopy, Nat. Photon. **15**, 720 (2021).

[108] D. G. Joshi, A. P. Schnyder, and S. Takei, Detecting end states of topological quantum paramagnets via spin Hall noise spectroscopy, Phys. Rev. B **98**, 064401 (2018).

[109] D. Bhowmick and P. Sengupta, Antichiral edge states in Heisenberg ferromagnet on a honeycomb lattice, Phys. Rev. B **101**, 195133 (2020).

[110] D. Boldrin, B. Fåk, M. Enderle, S. Bieri, J. Ollivier, S. Rols, P. Manuel, and A. S. Wills, Haydeeite: A spin-$\frac{1}{2}$ Kagome ferromagnet, Phys. Rev. B **91**, 220408(R) (2015).

[111] R. Chisnell, J. S. Helton, D. E. Freedman, D. K. Singh, F. Demmel, C. Stock, D. G. Nocera, and Y. S. Lee, Magnetic transitions in the topological magnon insulator Cu(1,3-bdc), Phys. Rev. B **93**, 214403 (2016).

[112] R. Chisnell, J. S. Helton, D. E. Freedman, D. K. Singh, R. I. Bewley, D. G. Nocera, and Y. S. Lee, Topological Magnon Bands in a Kagome Lattice Ferromagnet, Phys. Rev. Lett. **115**, 147201 (2015).